IEEE Access
Multidisciplinary | Rapid Review | Open Access Journal

Received July 17, 2020, accepted July 23, 2020, date of publication July 27, 2020, date of current version August 6, 2020.

Digital Object Identifier 10.1109/ACCESS.2020.3012030

Wideband THz Filtering by Graphene-Over-Dielectric Periodic Structures With and Without MgF_2 Defect Layer

M. POURMAND AND P. K. CHOUDHURY, (Senior Member, IEEE)
Institute of Microengineering and Nanoelectronics, Universiti Kebangsaan Malaysia (UKM), Bangi 43600, Malaysia

Corresponding author: P. K. Choudhury (pankaj@ukm.edu.my)

This work was supported in part by the Ministry of Higher Education (MOHE), Malaysia, under Grant FRGS/1/2019/STG02/UKM/01/1 and Grant AKU254.

ABSTRACT Investigation of the spectral response of graphene-dielectric (SiO_2)-based periodic structure was made in the far-infrared (IR) to the mid-IR frequency range, and the effects of different parametric and operational conditions on the transmission characteristics were explored. The presence of stop-bands, followed by Bragg reflection harmonics, in the low-frequency regime was observed exploiting the bilayer graphene (BLG) sheets. The width of stop-bands could be tuned by altering the number of periods as well as the chemical potential of BLG. The formation of a stop-band (with a transmission dip positioned at ∼16 THz) having a span of ∼3 THz was noticed, which is possibly a very large stop-bandwidth reported so far. The structure was also analyzed upon introducing a defect layer of MgF_2 having a thickness smaller than the dielectric medium. This results in shifting the position of stop-bands of the structure. The characteristics of transmission spectra were found to be greatly depending on the chemical potential (of BLG) and other operating conditions – the feature that triggers the usefulness of the proposed structure in the design of optical modulators, tunable narrow-band filters, broad-band reflectors and biosensing applications.

INDEX TERMS THz filters, complex mediums, multilayered structures, defect mediums.

I. INTRODUCTION

The propagation of electromagnetic waves through periodic structures have been of great importance as these exhibit photonic band-gaps where photons of particular frequencies cannot propagate – the feature that can be harnessed for multifarious technological applications, such as designing optical sensors, narrow-band optical sources, optical filters, one-dimensional (1D) photonic crystals, etc. [1]–[8]. Some other applications would include storage devices, solar cells, resonators, optical buffers and time-division multiplexers [10]–[13]. Within the context, the investigation of spectral characteristics of such periodic mediums remains important, that essentially includes the studies of transmission, reflection and absorption properties.

These periodic structures have been studied incorporating varieties of mediums as the properties of those can be exploited, along with the operating conditions, to exhibit the desired spectral features. Certain designs of these may even exhibit negative effective index [7], [14]. In this stream, graphene, being a gapless semiconductor, yields adjustable surface conductivity, high carrier mobility, thermal sensitivity and environmental stability, and therefore, it is widely used in designing nanocomposites [15]. In the context of photonics technology, graphene behaves extraordinarily, which makes it to be promising optical material [16]. For instance, the surface plasmons excited in graphene are confined much more strongly than those in noble metals, and can be coupled with electrons, photons or phonons [17]. Furthermore, the tunability of plasmons in graphene-based structures may be achieved with better ease because the charge carriers can be easily controlled by electrical gating and doping with low amount of loss [18]. These exotic characteristics allow graphene-based structures to be useful in designing metamaterials to realize varieties of optical components and/or devices [19]–[22].

The optical properties of engineered periodic mediums can be used for different photonic applications [23]–[26]. It has been reported before that graphene has the property

The associate editor coordinating the review of this manuscript and approving it for publication was Nicola Andriolli.

to enhance the absorption of light waves [27], [28]. Also, graphene-based nanostructured slab waveguides can sustain slow-light, and can be used to suppress the propagating modes [29]. Both these phenomena have great importance in photonics technology, as evidenced from [30], [31]. The incorporation of graphene in certain engineered metamaterials would increase plasmon-induced transparency [32].

Wide-bandwidth structures have been useful in many applications, such as multiplexers, absorbers, filters etc. [6], [14], [33]–[35]. Researchers have been involved in designing composite mediums and/or engineered structures that can exhibit wide-band features. Within the context, diverse avenues for electromagnetic research have emerged in the terahertz (THz) spectral regime. These include applications in sensing [36], [37], modulation [38], [39], signal processing [40], switching [41], antenna technology [44], spectroscopy [43], imaging [44], medical diagnostics [45], etc. Apart from these, THz metasurfaces are useful in designing absorbers [46] and filters [47].

The use of graphene in THz devices has been greatly interesting. In line with this, varieties of graphene-based THz absorbers have been reported in the literature [48]–[50]. In this communication, we investigate certain graphene-embedded periodic structures in respect of the transmission properties. In particular, we use periodic dielectric-graphene type of medium with the incorporation of bilayer graphene (BLG) and SiO_2 dielectric mediums. Within the context, the use of SiO_2 in the THz regime is common, not only for easy fabrication process, but also for its fairly low-loss property in the THz regime. The SiO_2 dielectric medium not only provides stable interaction with graphene sheets, but also exhibits relatively small tangent loss at THz frequencies [51], [52]. Exploiting the transfer-matrix method (TMM), we determine the transmission characteristics, which exhibit stop-bands in the low-frequency regime, as obtained under different parametric and operating conditions. In the later part of study, we deduce the transmission spectra in the situation when the periodic structure has a nanolayer of magnesium fluoride (MgF_2) as a defect medium, and observe the effect on the spectral features. It must be pointed out here that we use MgF_2 because of its being a low refractive index medium, and also, having a broad band transmission at THz frequencies [53]. The results reveal the presence of relatively wide stop-bands – the property that can be used in many photonic applications, such as wide-band filters, absorbers and biosensors. Within the context, graphene-based multilayer structures have potentials in designing modulators [54], [55]. Apart from this, the proposed dielectric-graphene kind of periodic multilayered structure can be considered as a 1D photonic crystal. Thus, the structure inherits the applications of such materials, as [56], [57] determine.

II. ANALYTICAL TREATMENT

We consider a periodic stack of SiO_2 dielectric and BLG sheets in which the topmost layer is a BLG medium, as shown in fig. 1. The unit cell of the periodic structure is comprised

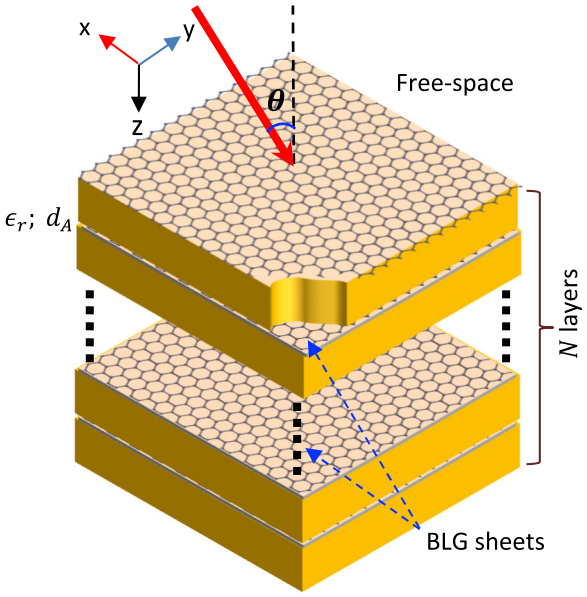

FIGURE 1. Schematic of the periodic structure comprised of BLG and SiO_2 mediums.

of a SiO_2 layer loaded with two graphene sheets. The SiO_2 medium has the relative permittivity ε_r and thickness d_A. Thus, the overall structure is the organization of $(N+1)$ BLG sheets sandwiching N number of SiO_2 layers.

The optical property of graphene greatly depends on the conductivity, which is a complex quantity of the form $\sigma(\omega, \mu_c) = \sigma' + j\sigma''$, wherein ω and μ_c are, respectively, the frequency and chemical potential. In the absence of magnetic bias and spatial dispersion, the conductivity σ of monolayer graphene is determined by the Kubo formula [29]:

$$\sigma(\omega, \mu_c) = \frac{2e^2 k_B T}{\pi\hbar^2}\left\{\frac{-j}{(\omega - j\gamma)}\right\}\ln\left\{2\cosh\left(\frac{\mu_c}{2k_B T}\right)\right\} - \frac{je^2}{4\pi\hbar}\ln\left\{\frac{2\mu_c - \hbar(\omega - j\gamma)}{2\mu_c + \hbar(\omega - j\gamma)}\right\} \quad (1)$$

where $\hbar\ (= h/2\pi)$ is the reduced Planck's constant, k_B is Boltzmann's constant, T is the absolute temperature, e is the electronic charge, and γ is the rate of scattering, which is inversely proportional to the electron relaxation time [58]. The two terms in eq. (1) relate to the intra- and inter-band transitions of charge carriers. The inter-band transition of electrons mainly happens at frequencies above the Pauli Blocking frequency (i.e., $\omega > 2\mu_c/\hbar$) [59], in the vicinity of which the real part (of the inter-band term) increases, and attains the universal value of conductivity $\sigma_0 = e^2/4\hbar$. It is noteworthy that the inter-band transitions dominate in the visible frequency range. On the other hand, the intra-band transitions significantly exceed the inter-band form in the frequency range of far-IR to the mid-IR – the frequency regime of prime focus of this paper. The contribution of the inter-band term in the 3–100 THz spectral range is always weak, which allows one to neglect this.

While analyzing the structure comprised of BLG layers, it is noteworthy that it can exist in two different forms,

namely the AA and AB. In the case of AA type, the layers are exactly aligned [60], whereas in the AB type, half of the atoms lie directly over the center of a hexagon in the lower graphene layer, and the remaining half (of the atoms) lie over an atom [61]. Lin *et al.* [62] showed the N-layer AA-stacked graphene sheets to have a band structure consisting of N Dirac bands which are shifted in energy. Consequently, the optical conductivity of an AA-stacked graphene in the THz region can be determined as

$$\sigma_{AA}(\omega) = \frac{2e^2 k_B T}{\pi \hbar^2 N}\left\{\frac{-j}{(\omega - j\gamma)}\right\} \sum_{m=1}^{N} \ln\left[2\cosh\left(\frac{\mu_c + 2\alpha_1 \cos m\pi / N + 1}{2k_B T}\right)\right] \quad (2)$$

with N as the number of graphene layers and α_1 as the interaction energy of misoriented (or AA-stacked) graphene layers. The value of α_1 is determined to be 217 meV, while the separation distance (of the AA-stacked layers) as 3.6Å [62]. The authors demonstrated that the results derived using this formula remains in good agreement with the experimentally obtained values.

The electromagnetic behavior of the proposed structure can be analyzed upon evaluating the relative permittivity characteristics. For this purpose, the effective medium approximation (EMA) can be applied to the unit cell (comprised of graphene-dielectric periodic mediums) of the structure of fig. 1. The use of EMA models the structure as a homogeneous uniaxial anisotropic medium having the effective permittivity tensor ϵ_{eff}, given as

$$\epsilon_{eff} = \epsilon_t\left(\hat{x}\hat{x} + \hat{y}\hat{y}\right) + \epsilon_\perp \hat{z}\hat{z} \quad (3)$$

In the analyses, we consider the normal component of permittivity $\epsilon_\perp = \epsilon_r$ owing to the thickness of graphene sheets being significantly less than that of the dielectric layer. As such, the normal component of electric field cannot excite electrical current. On the other hand, the transverse component of permittivity, parallel to the graphene layers, can be calculated as [63]

$$\epsilon_t = \epsilon_t' - j\epsilon_t'' = \epsilon_r - j\frac{\sigma(\omega, \mu_c)}{\omega\epsilon_0 d_A} \quad (4)$$

where ϵ_r and d_A are, respectively, the relative permittivity and thickness of dielectric medium; the meanings of other symbols are as stated above. As can be seen, the imaginary part of ϵ_t bears the surface conductivity of graphene $\sigma(\omega, \mu_c)$.

To study the propagation of electromagnetic waves through the proposed structure, varieties of methods have been employed. These include the theory of plane wave expansion [64], finite difference time/frequency domain [65], TMM [66], [67] and Green function method [16], [17]. Among these, the TMM has been exploited in most of the investigations owing to its simplicity and flexibility. Interestingly, the TMM can be used in isotropic as well as anisotropic mediums including disordered configurations, wherein the defect modes can be introduced with less complexity [68], [69].

We consider the incidence plane wave as comprised of the TE-polarization with $E = (0, E_y, 0)$, $H = (H_x, 0, H_z)$, and the TM-polarization with $E = (E_x, 0, E_z)$, $H = (0, H_y, 0)$ having different wave numbers [70], i.e.,

$$k_{ix}^2 + k_{iz}^2 = \epsilon_{i,t} k_0^2 \quad \text{(for TE-polarized incidence)} \quad (5)$$

$$\frac{k_{ix}^2}{\epsilon_{i,\perp}} + \frac{k_{iz}^2}{\epsilon_{i,t}} = k_0^2 \quad \text{(for TM-polarized incidence)} \quad (6)$$

In these equations, the subscript i represents the layer of the component mediums (i.e., G|A or defect), k_0 is the free-space wavenumber, k_{iz} is the wavenumber of the normal components, $k_{ix} = k_0 \sin\theta$ (θ being the angle of incidence), and the subscripts t, $\perp$, respectively, represent the transverse and perpendicular permittivity components.

Now, the incidence wave must follow the Maxwell's equations, and satisfies the boundary conditions at each layer. As such, for nonmagnetic mediums, two wave equations can be defined for each layer. The propagation of wave through the layer of thickness of d_i can be determined using a 2×2 matrix, i.e., the transfer matrix M_i. In line with this, we define M_i for each layer including the BLG sheet and dielectric medium, corresponding to the TE- and TM-polarizations, as follows [65]:

$$M_i = \begin{bmatrix} \cos(k_{iz} d_i) & -\frac{j}{p_i}\sin(k_{iz} d_i) \\ -j p_i \sin(k_{iz} d_i) & \cos(k_{iz} d_i) \end{bmatrix} \quad (7)$$

In eq. (7), d_i is the thickness of each layer, and p_i is determined by the wave polarization. It must be noted that the factors $\left(k_{iz}/\omega\mu_0\right)$ and $\left(k_{iz}/\omega\mu_0\epsilon_0\epsilon_i\right)$ stand in the cases of TE- and TM-polarizations, respectively; μ_0, ϵ_0, being the respective free-space permittivity and permeability, ϵ_i being the ith layer permittivity. Since the thickness of BLG (i.e., d_g) is extremely small, the transfer matrix components for the last BLG layer for both the polarizations is put as

$$M_g = \begin{bmatrix} 1 & 0 \\ -\sigma & q1 \end{bmatrix} \quad (8)$$

The total transfer matrix (M_{total}) of the structure (of fig. 1) is evaluated as

$$M_{total} = M_{\mathrm{G|A}}^N M_g = \begin{bmatrix} m_{11} & m_{12} \\ m_{21} & m_{22} \end{bmatrix} \quad (9)$$

where N is the total number of alternating G|A layers, m_{ij} are the transfer matrix components, and M_g and $M_{\mathrm{G|A}}$ are, respectively, the transfer matrix for the BLG and dielectric layers. Moreover, the total transfer matrix for a single-defect structure can be evaluated as

$$M_{total} = M_{\mathrm{G|A}}^N M_g M_{df} M_{\mathrm{G|A}}^N M_g = \begin{bmatrix} m_{11} & m_{12} \\ m_{21} & m_{22} \end{bmatrix} \quad (10)$$

In eq. (10), N is the number of periods of G|A layers on both sides of the defect layer, and M_{df} represents the transfer matrix for a defect layer.

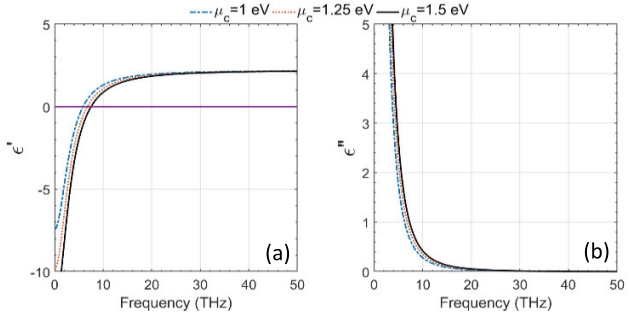

FIGURE 2. Frequency-dependence of effective permittivity; (a) real part and (b) imaginary part.

By exploiting the total transfer matrix in hand, we can evaluate the coefficients of reflection R and transmission T corresponding to the cases of TE- and TM-polarized incidence excitations. The expressions of these can be determined as [67]

$$R = |r|^2 = \left| \frac{(m_{11} + m_{12}p_{N+1})\,p_0 - m_{21} - m_{22}p_{N+1}}{(m_{11} + m_{12}p_{N+1})\,p_0 + m_{21} + m_{22}p_{N+1}} \right|^2 \quad (11)$$

$$T = \begin{cases} \left| \dfrac{2p_0}{(m_{11}+m_{12}p_{N+1})\,p_0+m_{21}+m_{22}p_{N+1}} \right|^2 & (\text{forTE}) \\ \dfrac{p_0}{p_{N+1}} \left| \dfrac{2p_0}{(m_{11}+m_{12}p_{N+1})\,p_0+m_{21}+m_{22}p_{N+1}} \right|^2 & (\text{forTM}) \end{cases} \quad (12)$$

In eqs. (11) and (12), $p_0 = \sqrt{\varepsilon_0}/\mu_0 \cos\theta_0$ and $p_{N+1} = \sqrt{\varepsilon_{N+1}}/\mu_{N+1} \cos\theta_{N+1}$ in the case of TE-polarization, whereas corresponding to the TM-polarized incidence, we have $p_0 = \left(\sqrt{\varepsilon_0}/\mu_0\right)/\cos\theta_0$ and $p_{N+1} = \left(\sqrt{\varepsilon_{N+1}}/\mu_{N+1}\right)/\cos\theta_{N+1}$. Here the subscripts $N+1$ and 0 represent the input and output layers, respectively. Also, ε_{N+1} and μ_{N+1} are the relative permittivity and relative permeability values, respectively, and θ_{N+1} is the angle formed at the output layer. As to the absorption of incidence radiation, it happens when the light impinges on the top surface. However, some portion of light, in general, is transmitted and/or reflected. This allows the absorption coefficient to be stated in the form $A(\lambda) = 1-[T(\lambda) + R(\lambda)]$; $T(\lambda)$ and $R(\lambda)$ being the wavelength-dependent transmission and reflection coefficients, respectively. Exploiting eqs. (11) and (12), one may evaluate the spectral characteristics of the proposed structure.

III. RESULTS AND DISCUSSION

The electromagnetic behavior of BLG deposited over a dielectric medium can be understood by studying the frequency-dependence of relative permittivity. To observe this, we assume the SiO_2 dielectric layer to have the relative permittivity and thickness values as $\epsilon_r = 2.25$ and $d_A = 6.9$ μm, respectively. As shown in fig. 1, the dielectric layers are sandwiched between two BLG sheets having the thickness $d_g = 0.9$ nm. Figures 2a and 2b, respectively, illustrate the frequency dependence of the real (ϵ') and imaginary (ϵ'') parts of transverse permittivity ϵ_t for a BLG sheet deposited over the aforementioned kind of dielectric layer, as deduced upon exploiting the EMA. These plots are obtained for the frequency span of 0–50 THz, and using the different values of chemical potential μ_c of graphene, namely 1.0 eV, 1.25 eV and 1.5 eV. We also use the other operational values as $\gamma = 1.32$ meV and $T = 300$ K.

At this point, it is worth to mention that Rodrigo *et al.* [71] reported before that multilayer graphene sheets with a separation distance (among the used monolayer sheets) of 1 nm provide broader tunability than a monolayer graphene sheet. The separation was chosen to be less than 1 nm, in order to neglect the interlayer interactions. They experimentally proved that the biasing in multilayer graphene is more effective than in monolayer graphene. Further, the Fermi energy E_f of monolayer graphene can be tuned from 0.2 eV to 1.2 eV [72]. It was proved that, in a BLG structure, a two-fold carrier density n_s can be obtained using the same amount of biasing as used in the case of monolayer sheet. Recalling the relation $E_f \approx \sqrt{n_s}$, the same Fermi energy, as in monolayer graphene, can be obtained in BLG with a considerably low bias [71].

We observe in fig. 2 that the real part ϵ' exhibits the positive and negative dependence on the operating frequency (fig. 2a), whereas the imaginary part ϵ'' is positive-valued only (fig. 2b). The characteristics of effective permittivity greatly depend on the value of μ_c – the feature which is relatively more prominent for ϵ' (fig. 2a). We notice that ϵ' shows sharp increase (from negative values) for a small change in frequency from 0–6 THz, and above 6 THz, it becomes small positive-valued with nerly saturation in the frequency span of ∼30–50 THz. We clearly observe in fig. 2a that the increase in μ_c results in ϵ' to be negative-valued over a relatively larger frequency range. For instance, corresponding to $\mu_c = 1.0$ eV, ϵ' becomes negative at ∼5.5 THz, whereas the use of $\mu_c = 1.5$ eV increases this frequency value to ∼8.0 THz. The values of ϵ'', however, show sharp decrease in the low-frequency regime, and become almost vanishing above 30 THz.

When the BLG sheet has a sufficiently negative susceptance (i.e., $\sigma'' < -\omega\epsilon_o\epsilon_r d_A$), the extraordinary waves are only allowed to propagate through the structure. In that case, ϵ_t has a negative real part, but the normal component of relative permittivity is positive (i.e., $\epsilon_\perp > 0$). In this condition, the TE-polarized waves are mainly evanescent, whereas the TM-polarized ones are allowed to propagate with the transverse wavenumber $k_t > \sqrt{\omega\epsilon_o\epsilon_r}$, though those are evanescent in free-space. Moreover, the zero-crossing frequency of ϵ_t' occurs when $\sigma'' = -\omega\epsilon_o\epsilon_r d_A$, which depends on μ_c as well. We observe in fig. 2 that the zero-crossing frequencies occur at nearly 5.7 THz, 6.7 THz, and 7.7 THz corresponding to the values of μ_c as 1.0 eV, 1.25 eV and 1.5 eV, respectively. Beyond these values of frequency, and upon reaching the Pauli blocking frequencies at $\omega = 2\mu_c/\hbar$, waves can propagate through the structure with low loss. Finally, the real part of transverse permittivity ϵ_t' approaches the dielectric permittivity at high frequencies due to a lower contribution of the BLG conductivity compared to ϵ_r.

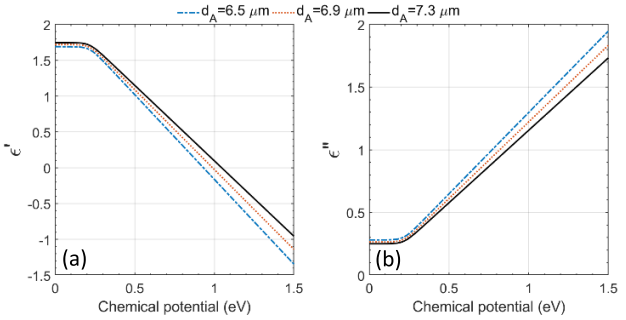

FIGURE 3. Effective permittivity vs. chemical potential plots for different values of dielectric layer thickness d_A; (a) real part and (b) imaginary part.

Indeed, the thickness d_A (of dielectric medium) and chemical potential μ_c (of BLG medium) will essentially affect the effective permittivity values. To determine this, we plot ϵ' and ϵ'' against μ_c for three illustrative values of d_A, namely 6.5 μm, 6.9 μm and 7.3 μm; fig. 3 shows the obtained results. From this figure, we observe the relationships to be nearly of the forms $\epsilon' \propto \mu_c^{-1}$ and $\epsilon'' \propto \mu_c$, which hold for $\mu_c = 0.2$ eV and above. Further, the increase in d_A makes ϵ' to increase a little, whereas ϵ'' is slightly decreased; the difference remains more for larger values of μ_c.

We now attempt to observe the effect of BLG sheets on the transmission characteristics of the proposed multilayer structure. For this purpose, we compare the results obtained in the case when graphene sheets are not incorporated in the configuration. This makes the structure to assume the form as if the SiO_2 dielectric slabs are standing in the free-space at a periodic distance. Considering the related parametric values as $\epsilon_r = 2.2$ and $d_A = 6.9$ μm, fig. 4a shows the frequency-dependence of transmission (T), reflection (R) and absorption (A) of the structure in the absence of BLG sheets. Figure 4b exhibits these plots when the free-space is occupied with the BLG medium, considering μ_c to be 1.0 eV. The unit cell structure is shown in fig. 1., which is of the $(\mathrm{G}\,|\,\mathrm{A})^{\mathrm{N}}\,\mathrm{G}$ kind. In both the situations, we choose the operating frequency range to be 0–50 THz, and the incidence happens at $\theta = 0°$ (i.e., the case of normal incidence).

Upon exploiting the TMM with the chosen design parameters, we observe in fig. 4a the absorption to be nearly vanishing throughout the used frequency range. Also, the transmission and reflection spectra are periodic in nature, which is very much expected due to Bragg reflections from a band-gap medium. The amount of transmission remains large, whereas the reflection is small, and the transmission maxima corresponds to the reflection minima.

The spectral characteristics are drastically altered upon incorporating BLG layers in the structure (replacing the free-space), as can be seen in fig. 4b. We now clearly observe the presence of a stop-band at low frequency regime, where graphene can be considered to behave as ultrathin metallic sheet in the unit cell. This is very much justified due to certain amount absorption happening at low frequencies. At higher frequencies, however, Bragg reflections occur with the peak transmission exhibiting slow increase with

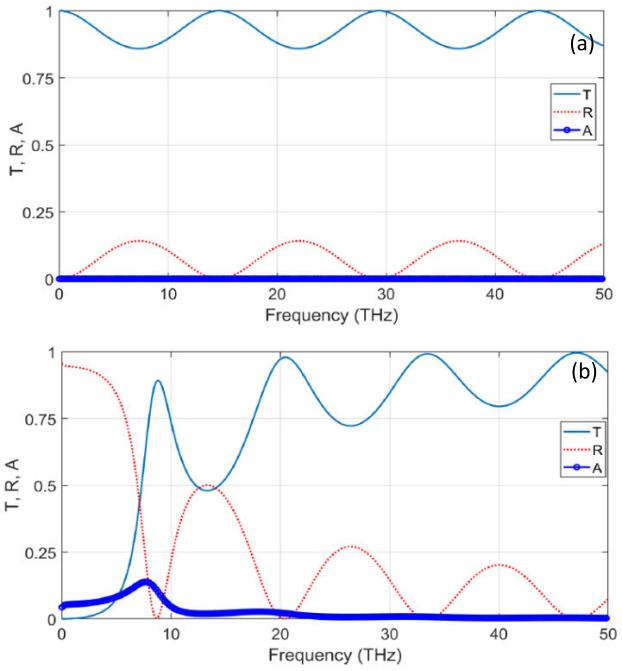

FIGURE 4. Frequency-dependence of transmission, reflection and absorption without (a) and with (b) the presence of BLG sheets in multilayer configuration.

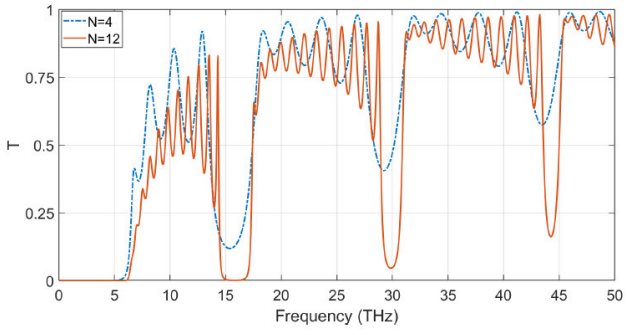

FIGURE 5. Frequency-dependence of transmission by the $(G\,|\,A)^N\,G$ structure corresponding to the values of $N = 4$, $N = 12$.

increasing frequency. The reflection and transmission spectra complement each other. We also notice that the spectral characteristics remain unaltered for both the TM- and TE-polarized incidence excitations.

To further investigate the presence of stop-bands, we deduce the transmission properties for different number of periods N in the $(\mathrm{G}\,|\,\mathrm{A})^N\,\mathrm{G}$ configuration, taking into account the normal incidence of waves and $\mu_c = 1.0$ eV. Figure 5 shows the transmission spectra in the 0–50 THz range, considering $N = 4$ and $N = 12$, and also, $d_A = 6.9$ μm. It is worth to mention at this point that the process of chemical vapor deposition (CVD) is generally deployed in synthesis, in order to realize multilayer graphene-dielectric kind of structure. This has been comprehensively explained in [62].

The obtained plots in fig. 5 determine small enhancements in the width as well as the number of stop-bands with the

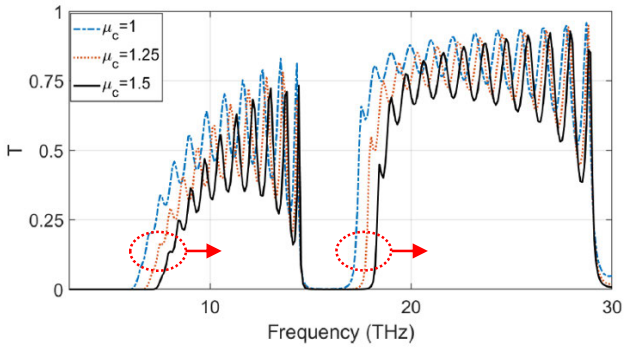

FIGURE 6. Frequency-dependence of transmission by the $(G\,|\,A)^N\,G$ structure corresponding to the μ_c -values as 1.0 eV, 1.25 eV and 1.50 eV, and $N = 12$.

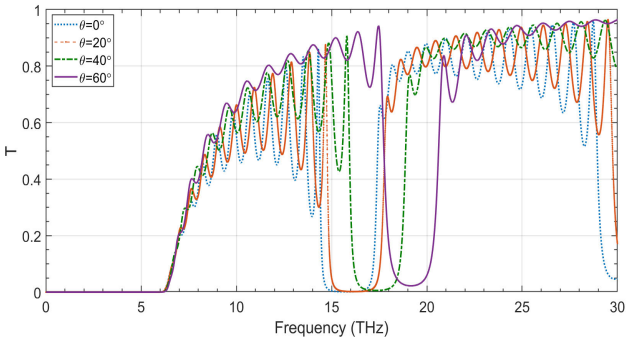

FIGURE 7. Transmission spectra for different values of incidence angle, viz. 0°, 20°, 40° and 60°.

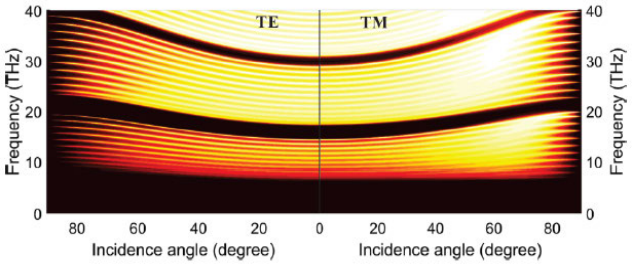

FIGURE 8. Transmission spectra for different values of incidence angle considering the TE-(left-panel) and TM-polarized (right-panel) incidence excitations.

increase in the number of periods used in multilayer configuration. The band-gaps basically appear at the low frequency regime; the increase in frequency results in partial Bragg reflections followed by harmonics. Also, the number of transmission peaks is determined by the period N; the more the value of N is, the more becomes the transmission peaks. We also notice that the level of transmission is considerably lower, as compared to the case of without using BLG, and these are mostly determined by the number of periods. This is attributed to the phenomenon that BLG behaves like a metallic sheet in the region between the first and second stop-bands with the surface impedance of $Z_s = 1/\sigma$. The greater the number of periods is, the less is the transmission level.

In order to observe the effect of chemical potential on the transmission characteristics, we use three different values of μ_c, namely 1.0 eV, 1.25 eV and 1.50 eV, and plot the transmission spectra considering the normal incidence and $N = 12$. The other geometrical parameters are kept the same; fig. 6 depicts the obtained results. This figure makes it clear that the increase in μ_c results in increase in the stop-band width, thereby allowing the structure to attain tunability characteristic. In this process, for each stop-band, the position of low-frequency edge remains unchanged, whereas that of the higher frequency edge increases.

To be more explicit, fig. 6 shows that the case of $\mu_c = 1.0$ eV yields the width of the first stop-band to be about 4.5 THz, which increases to ∼6 THz corresponding to $\mu_c = 1.5$ eV. Similarly, for the second stop-band, the choice of $\mu_c = 1.0$ eV gives the width to be ∼2 THz, which increases to about 3 THz when $\mu_c = 1.5$ eV. Such a size of stop-band is relatively broad among those reported in recent investigations. However, the value of chemical potential μ_c can be adjusted to the extent of empirical limitations of applying the electrostatic potential to the dielectric layer in the structure.

The afore discussed results are all obtained for normal incidence of waves. We now look at the angular dependence of transmission spectra. In this stream, fig. 7 depicts the spectral patterns corresponding to the incidence angles θ as 0° (normal incidence), 20°, 40° and 60° in the frequency range of 0–30 THz. We keep the value of μ_c to be 1.0 eV, and the other design parameters are left unchanged. We notice in this figure that the change in obliquity has two-fold impact – altering the position as well as the width of stop-band. Figure 7 exhibits explicitly that the increase in incidence angle causes blue-shifts in the position of stop-band. Also, the increase in θ from 0° to 60° introduces enhancement of about 1 THz in the width of stop-band.

In order to have deeper insight into the spectral characteristics of transmission in terms of its dependence on the incidence angle, we plot the same by sweeping θ in the range of 0° to 90°; fig. 8 depicts the obtained spectrum corresponding to the TE- and TM-polarized incidence excitations, keeping the parametric and operational conditions unchanged. We clearly notice that the transmission spectra for both the polarizations react similarly to the alterations in the angle of incidence. In this figure, the dark areas represent the forbidden frequencies. As can be seen in fig. 8, the stop-bands move slightly toward higher frequencies (i.e., undergo blue-shifts) as the incidence angle approaches nearly grazing condition. As such, the stop-band of $(G\,|\,A)^N\,G$ kind of structure can be tuned by altering the obliquity of incidence. However, the transmissions in both the polarizations become suppressed for angles larger than 65°.

We discussed so far the transmission properties of $(G\,|\,A)^N\,G$ kind of structure under certain parametric and operational conditions so that wide stop-bands can be achieved. The next step is to study the transmission properties of a defective structure. That is, we deliberately introduce a defect layer of certain thickness d_D and relative permittivity

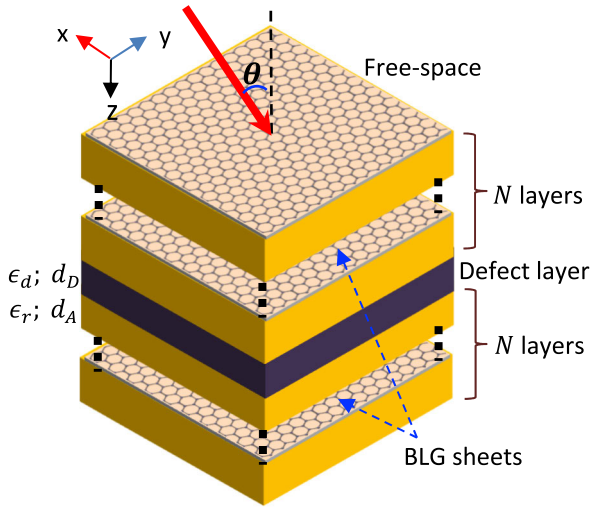

FIGURE 9. Schematic of multilayer graphene-dielectric structure with a defect layer of MgF_2 at the mid-point.

ε_d at the mid-point of the total number of (G | A) periods used in the configuration, as shown in fig. 9. This will essentially originate the defect mode as the periodicity of structure is perturbed [73]. Indeed, the characteristics of defect modes can be used to tune the transmission properties of the structure. According to Bloch theory, the defect modes, which satisfy Bloch condition $\cos(Kd_D) > 1$ (K being the wavenumber), can propagate in band-gaps. Since Kd_D is intrinsically periodic, upon increasing the defect layer thickness d_D to that of the dielectric layer d_A, the defect mode would disappear. However, for $d_D > d_A$, it will be generated again. We now simulate the effect of variations in defect layer in the first allowed band of transmission.

As a defect layer, we use MgF_2 having thickness $d_D = 5.8\ \mu$m and dielectric constant $\epsilon_d = 1.9$. Thus, the structure now assumes the form of $(G\,|\,A)^N\,GD\,(G\,|\,A)^N\,G$, which we analyze considering $N = 6$. As such, with reference to fig. 9, the structure has 13 layers altogether, and the defect layer is introduced at the mid-point. Since d_D essentially increases the device length, we first investigate the effect of variations in d_D on the spectral properties of defect modes, exploiting the TMM, and considering the normal incidence of TM-polarized waves (fig. 9). Figure 10 illustrates the obtained results, wherein we plot the defect mode central frequency and transmission peak against the thickness d_D of defect layer, which we vary from 2 μm to 7 μm. Also, we keep the chemical potential $\mu_c = 1.0$ eV. In this figure, the blue error bars show the full-width half-maximum (FWHM) of the central frequency of defect mode.

We observe in fig. 10 that the defect mode frequency decreases with the increase in d_D. This demonstrates that the modes with constant Kd_D are allowed to propagate. We also see in fig. 10 that the FWHM and maximum transmission peak of the defect mode follow the same high and low changes. The defect modes propagating at the center of stop-band exhibit the least values of FWHM as well as transmission peak levels compared to those propagate at the

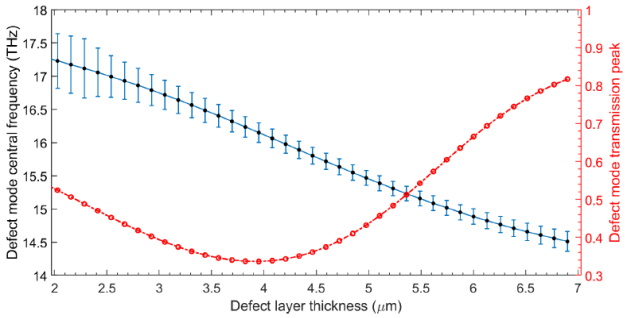

FIGURE 10. Spectral properties of defect mode for different values of defect layer thickness d_D.

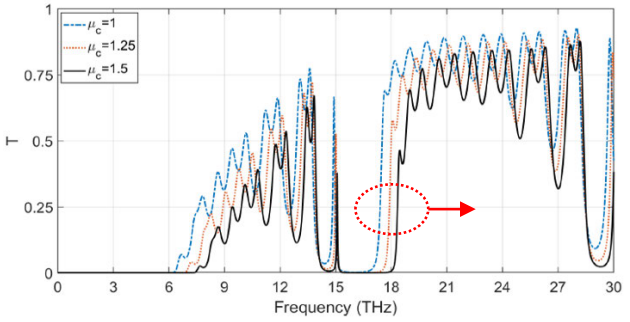

FIGURE 11. Frequency-dependence of transmission corresponding to the μ_c-values as 1.0 eV, 1.25 eV and 1.50 eV using $N = 6$.

edge of stop-band. We choose the defect layer thickness $d_D = 5.8\ \mu$m, which corresponds to the central frequency of defect mode to be $f_D = 15.02$ THz and the FWHM to be 0.228 THz; we use these parametric and operational conditions in further analyses.

We now examine the tunability of the proposed structure by altering the chemical potential μ_c. Figure 11 demonstrates the transmittance spectra of defect modes for three different values of μ_c, viz. 1.0 eV, 1.25 eV and 1.50 eV. Similar to what observed before in fig. 6, we find that the increase in μ_c results in larger width of the stop-band, and the position of defect mode moves toward higher frequencies. Also, the peaks are suppressed due to high reflections as these move near the center of stop-band. We clearly notice in fig. 11 that the use of $\mu_c = 1.5$ eV yields the stop-band to be of over 3 THz width.

Figure 12 makes the effect of chemical potential on the transmission characteristics of defect modes more explicit. In this figure, we plot the central frequency and peak transmission of defect modes against μ_c, and the blue error bars indicate the FWHM of the defect mode central frequency. We see that the stop-band is continuously sketching toward high frequencies with the higher values of μ_c. On the other hand, the defect mode frequency and FWHM tend to decrease, and the transmission peak level gets smaller values. This is attributed to the fact that the increase in μ_c makes the imaginary part of $\sigma(\omega)$ to be larger, thereby making the defect mode peak transmission to be reduced. This property

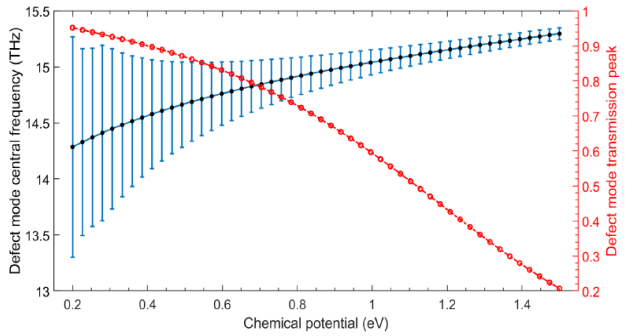

FIGURE 12. Defect mode central frequency and peak transmission for different values of μ_c ranging from 0.2 eV to 1.5 eV.

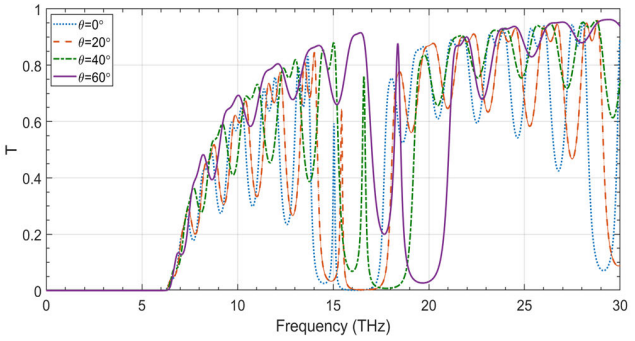

FIGURE 13. Transmission spectra of defect mode for different values of incidence obliquity.

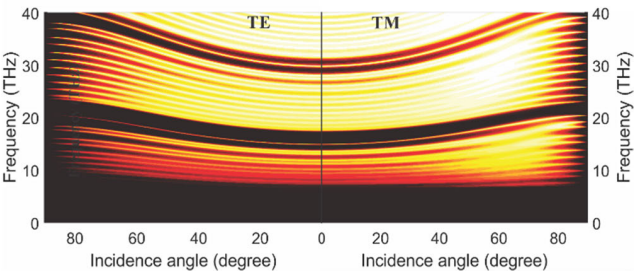

FIGURE 14. Transmission spectra of defect modes for different values of incidence angle considering the TE- (left panel) and TM-polarized (right panel) incidence excitations.

can be used in designing tunable filters in the THz regime of the electromagnetic spectrum.

Lastly, we focus on the effect of incidence obliquity on the transmission spectra of defect modes. Figure 13 illustrates such plots for the incidence angle θ having the discrete values 0°, 20°, 40° and 60° under the circumstance when $\mu_c = 1.0$ eV. We see that the increase in angle shifts the position of stop-bands toward the higher frequency end, i.e., the transmission minima undergo blue-shifts for increased obliquity.

To get a deeper insight into the angular dependence of the proposed MgF_2 defect-based structure, we plot the transmission spectra corresponding to both the TE- and TM-polarized incidence excitations for different values of obliquity ranging from 0° to 90°, while keeping the other parametric and operational conditions unchanged; fig. 14 depicts the obtained results (for the cases of TE- and TM-polarizations on the left- and right-panels, respectively). This figure clearly shows that, as the angle of incidence increases, the transmission spectra undergo small shifts toward higher frequencies. The defect mode exists upon reaching the angle larger than 65° for both the kinds of polarization. However, the defect mode disappears as the other propagating modes enter the band gap of the structure. Figure 14 shows that the defect mode is more resilience to the incidence angle in the case of TM-polarized excitation. The study essentially yields that the defect mode and its characteristics can be tuned by changing the incidence obliquity, which adds more tunability property to the proposed structure, apart from the use of chemical potential of BLG used in the design.

IV. CONCLUSION

From the above discussed results, it can be inferred that the optical response of periodic arrangement of dielectric and BLG sheets exhibits almost similar spectral features for the TE- and TM-polarized incidence excitations. The use of BLG medium in the structure results in the presence of stop-band at low frequency regime followed by Bragg reflection harmonics. The width and position of stop-bands can be governed by suitably controlling the chemical potential (of graphene) and incidence obliquity. Apart from these, the number of periods in the structure also affects the spectral performance; the higher number of periods yields relatively wider stop-bandwidth. The results demonstrate that using 12 periods of BLG-over-dielectric mediums and the chemical potential of 1.0 eV can provide a stop-band (with a transmission dip at ∼16 THz) with a span of ∼3 THz, which is fairly large. The obtained spectral response in the case of incorporating defect mode, as created by placing a layer of MgF_2 (of thickness smaller than that of the dielectric layer) in the middle of periodic arrangement, shows alterations in the transmission characteristics. This essentially depends on the presence of defect mode, and can be governed by the external operating conditions, such as the graphene Fermi energy and incidence obliquity. The increase in chemical potential results in relatively wider stop-band. The obtained results indicate the usefulness of the structure in various photonic applications, such as tunable wide-band filters, absorbers and biosensors. Apart from these, multilayer graphene-based structures can be used in designing optical modulators [54], [55] as well.

ACKNOWLEDGMENT

The authors are thankful to the 3 anonymous reviewers for constructive criticisms on the manuscript.

REFERENCES

[1] A. M. A. Ibrahim and P. K. Choudhury, "On the Maxwell-duffing approach to model photonic deflection sensor," *IEEE Photon. J.*, vol. 5, no. 4, Aug. 2013, Art. no. 6800812.
[2] M. Bellingeri and F. Scotognella, "The influence of a power law distribution of cluster size on the light transmission of disordered 1-D photonic structures," *J. Lightw. Technol.*, vol. 33, no. 19, pp. 3980–3985, Oct. 1, 2015.
[3] C.-H. Yeh, N. Tsai, Y.-H. Zhuang, C.-W. Chow, and W.-F. Liu, "Fault self-detection technique in fiber Bragg grating-based passive sensor network," *IEEE Sensors J.*, vol. 16, no. 22, pp. 8070–8074, Nov. 2016.

[4] M. Lindner, E. Tunc, K. Weraneck, F. Heilmeier, W. Volk, M. Jakobi, A. W. Koch, and J. Roths, "Regenerated Bragg grating sensor array for temperature measurements during an aluminum casting process," *IEEE Sensors J.*, vol. 18, no. 13, pp. 5352–5360, Jul. 2018.

[5] R. Bandyopadhyay and R. Chakraborty, "Transmission filters utilizing cavity resonances in bandgap-engineered monomaterials," *IEEE Photon. Technol. Lett.*, vol. 30, no. 2, pp. 189–192, Jan. 15, 2018.

[6] N. Iqbal and P. K. Choudhury, "Mode filtering aspects of periodic multi-layered chiro-ferrite medium," *Optik*, vol. 157, pp. 449–454, Mar. 2018.

[7] K. V. Sreekanth, P. Mahalakshmi, S. Han, M. S. M. Rajan, P. K. Choudhury, and R. Singh, "Brewster mode-enhanced sensing with hyperbolic metamaterial," *Adv. Opt. Mater.*, vol. 7, no. 21, pp. 1900680-1–1900680-6, 2019.

[8] S. Tang, R. Wang, and J. Han, "Directional transmission characteristics of acoustic waves based on artificial periodic structures," *IEEE Access*, vol. 7, pp. 94033–94038, 2019.

[9] S. Ceccuzzi, P. Baccarelli, C. Ponti, and G. Schettini, "Effect of source position on directive radiation in EBG structures with epsilon-near-zero behavior," *IEEE Antennas Wireless Propag. Lett.*, vol. 18, no. 6, pp. 1253–1257, Jun. 2019.

[10] O. Painter, R. K. Lee, A. Scherer, A. Yariv, J. D. O'Brien, P. D. Dapkus, and I. I. Kim, "Two-dimensional photonic band-gap defect mode laser," *Science*, vol. 284, no. 5421, pp. 1819–1821, Jun. 1999.

[11] G. Alagappan, X. W. Sun, P. Shum, M. B. Yu, and M. T. Doan, "One-dimensional anisotropic photonic crystal with a tunable bandgap," *J. Opt. Soc. Amer. B, Opt. Phys.*, vol. 23, no. 1, pp. 159–167, 2006.

[12] J. Cos, J. Ferre-Borrull, J. Pallares, and L. F. Marsal, "Tunable Fabry–Pérot filter based on one-dimensional photonic crystals with liquid crystal components," *Opt. Commun.*, vol. 282, no. 6, pp. 1220–1225, Mar. 2009.

[13] A. Banerjee, "Novel applications of one-dimensional photonic crystal in optical buffering and optical time division multiplexing," *Optik*, vol. 122, no. 4, pp. 355–357, Feb. 2011.

[14] M. A. Baqir and P. K. Choudhury, "Hyperbolic metamaterial-based UV absorber," *IEEE Photon. Technol. Lett.*, vol. 29, no. 18, pp. 1548–1551, Sep. 15, 2017.

[15] S. Bellucci, A. Maffucci, S. Maksimenko, F. Micciulla, M. Migliore, A. Paddubskaya, D. Pinchera, and F. Schettino, "Electrical permittivity and conductivity of a graphene nanoplatelet contact in the microwave range," *Materials*, vol. 11, no. 12, Dec. 2018, Art. no. 2519.

[16] A. N. Grigorenko, M. Polini, and K. S. Novoselov, "Graphene plasmonics," *Nature Photon.*, vol. 6, pp. 749–758, Nov. 2012.

[17] F. H. L. Koppens, D. E. Chang, and F. J. G. de Abajo, "Graphene plasmonics: A platform for strong Light–Matter interactions," *Nano Lett.*, vol. 11, no. 8, pp. 3370–3377, Aug. 2011.

[18] Z. Fang, Y. Wang, Z. Liu, A. Schlather, P. M. Ajayan, F. H. L. Koppens, P. Nordlander, and N. J. Halas, "Plasmon-induced doping of graphene," *ACS Nano*, vol. 6, no. 11, pp. 10222–10228, Nov. 2012.

[19] J. T. Kim and C. G. Choi, "Graphene-based polymer waveguide polarizer," *Opt. Express*, vol. 20, no. 4, pp. 3556–3562, 2012.

[20] W. B. Lu, W. Zhu, H. J. Xu, Z. H. Ni, Z. G. Dong, and T. J. Cui, "Flexible transformation plasmonics using graphene," *Opt. Express*, vol. 21, no. 9, pp. 10475–10482, 2013.

[21] M. Ghorbanzadeh, S. Darbari, and M. K. Moravvej-Farshi, "Graphene-based plasmonic force switch," *Appl. Phys. Lett.*, vol. 108, no. 11, Mar. 2016, Art. no. 111105.

[22] B. Zeng, Z. Huang, A. Singh, Y. Yao, A. K. Azad, A. D. Mohite, A. J. Taylor, D. R. Smith, and H.-T. Chen, "Hybrid graphene metasurfaces for high-speed mid-infrared light modulation and single-pixel imaging," *Light, Sci. Appl.*, vol. 7, no. 1, 2018, Art. no. 51.

[23] M. Fehrenbacher, S. Winnerl, H. Schneider, J. Döring, S. C. Kehr, L. M. Eng, Y. Huo, O. G. Schmidt, K. Yao, Y. Liu, and M. Helm, "Plasmonic superlensing in doped GaAs," *Nano Lett.*, vol. 15, no. 2, pp. 1057–1061, Feb. 2015.

[24] L. Xie, W. Gao, J. Shu, Y. Ying, and J. Kono, "Extraordinary sensitivity enhancement by metasurfaces in terahertz detection of antibiotics," *Sci. Rep.*, vol. 5, no. 1, pp. 1–4, Aug. 2015.

[25] M. Ghasemi, P. K. Choudhury, and A. Dehzangi, "Nanoengineered thin films of copper for the optical monitoring of urine—A comparative study of the helical and columnar nanostructures," *J. Electromagn. Waves Appl.*, vol. 29, no. 17, pp. 2321–2329, Nov. 2015.

[26] A. Farmani, A. Zarifkar, M. H. Sheikhi, and M. Miri, "Design of a tunable graphene plasmonic-on-white graphene switch at infrared range," *Superlattices Microstruct.*, vol. 112, pp. 404–414, Dec. 2017.

[27] A. Y. Nikitin, F. Guinea, F. J. Garcia-Vidal, and L. Martin-Moreno, "Surface plasmon enhanced absorption and suppressed transmission in periodic arrays of graphene ribbons," *Phys. Rev. B, Condens. Matter*, vol. 85, no. 8, Feb. 2012, Art. no. 081405.

[28] J.-T. Liu, N.-H. Liu, J. Li, X. Jing Li, and J.-H. Huang, "Enhanced absorption of graphene with one-dimensional photonic crystal," *Appl. Phys. Lett.*, vol. 101, no. 5, Jul. 2012, Art. no. 052104.

[29] M. A. Baqir and P. K. Choudhury, "Graphene-based slab waveguide for slow-light propagation and mode filtering," *J. Electromagn. Waves Appl.*, vol. 31, no. 18, pp. 2055–2063, Dec. 2017.

[30] G. Wang, H. Lu, and X. Liu, "Dispersionless slow light in NIM waveguide based on a plasmonic analogue of electromagnetically induced transparency," *Opt. Express*, vol. 20, no. 19, pp. 20902–20907, 2012.

[31] J. Wang, B. Yuan, C. Fan, J. He, P. Ding, Q. Xue, and E. Liang, "A novel planar metamaterial design for electromagnetically induced transparency and slow light," *Opt. Express*, vol. 21, no. 21, pp. 25159–25166, 2013.

[32] M. A. Baqir, A. Farmani, P. K. Choudhury, T. Younas, J. Arshad, A. Mir, and S. Karimi, "Tunable plasmon induced transparency in graphene and hyperbolic metamaterial-based structure," *IEEE Photon. J.*, vol. 11, no. 4, pp. 4601510-1–4601510-10, Aug. 2019.

[33] C. Carceller, P. Soto, V. Boria, M. Guglielmi, and J. Gil, "Design of compact wideband manifold-coupled multiplexers," *IEEE Trans. Microw. Theory Techn.*, vol. 63, no. 10, pp. 3398–3407, Oct. 2015.

[34] M. A. Baqir and P. K. Choudhury, "Design of hyperbolic metamaterial-based absorber comprised of ti nanospheres," *IEEE Photon. Technol. Lett.*, vol. 31, no. 10, pp. 735–738, May 15, 2019.

[35] Y. Mori, E. Honda, R. Shiraki, K. Suzuki, H. Matsuura, H. Kawashima, S. Namiki, K. Ikeda, and K.-I. Sato, "Wavelength-division demultiplexing enhanced by silicon-photonic tunable filters in ultra-wideband optical-path networks," *J. Lightw. Technol.*, vol. 38, no. 5, pp. 1002–1009, Mar. 1, 2020.

[36] S. R. J. Bhatt, P. Bhatt, P. Deshmukh, B. R. Sangala, M. N. Satyanarayan, G. Umesh, and S. S. Prabhu, "Resonant terahertz InSb waveguide device for sensing polymers," *J. Infr., Millim., Terahertz Waves*, vol. 37, no. 8, pp. 795–804, Aug. 2016.

[37] F. Zangeneh-Nejad and R. Safian, "A graphene-based THz ring resonator for label-free sensing," *IEEE Sensors J.*, vol. 16, no. 11, pp. 4338–4344, Jun. 2016.

[38] M. Rahm, J.-S. Li, and W. J. Padilla, "THz wave modulators: A brief review on different modulation techniques," *J. Infr., Millim., THz Waves*, vol. 34, no. 1, pp. 1–27, Jan. 2013.

[39] W. Min, H. Sun, Q. Zhang, H. Ding, W. Shen, and X. Sun, "A novel dual-band terahertz metamaterial modulator," *J. Opt.*, vol. 18, no. 6, Jun. 2016, Art. no. 065103.

[40] K. S. Reichel, N. Lozada-Smith, I. D. Joshipura, J. Ma, R. Shrestha, R. Mendis, M. D. Dickey, and D. M. Mittleman, "Electrically reconfigurable terahertz signal processing devices using liquid metal components," *Nature Commun.*, vol. 9, no. 1, Dec. 2018, Art. no. 4202.

[41] M. Yarahmadi, M. K. Moravvej-Farshi, and L. Yousefi, "Subwavelength graphene-based plasmonic THz switches and logic gates," *IEEE Trans. THz Sci. Technol.*, vol. 5, no. 5, pp. 725–731, Sep. 2015.

[42] F. Zangeneh-Nejad and R. Safian, "Significant enhancement in the efficiency of photoconductive antennas using a hybrid graphene molybdenum disulphide structure," *J. Nanophotonics*, vol. 10, no. 3, Jul. 2016, Art. no. 036005.

[43] J. Qin, L. Xie, and Y. Ying, "A high-sensitivity terahertz spectroscopy technology for tetracycline hydrochloride detection using metamaterials," *Food Chem.*, vol. 211, pp. 300–305, Nov. 2016.

[44] A. Arbabi, E. Arbabi, S. M. Kamali, Y. Horie, S. Han, and A. Faraon, "Miniature optical planar camera based on a wide-angle metasurface doublet corrected for monochromatic aberrations," *Nature Commun.*, vol. 7, no. 1, Dec. 2016, Art. no. 13682.

[45] S. K. Yngvesson, A. Karellas, S. S. Glick, A. Khan, P. R. Siqueira, P. A. Kelly, and B. S. Peter, "Breast cancer margin detection with a single frequency terahertz imaging system," *Proc. SPIE*, vol. 9706, Mar. 2016, Art. no. 970603.

[46] X. Liu, I. V. Shadrivov, K. Fan, and W. J. Padilla, "Experimental realization of a terahertz all-dielectric metasurface absorber," *Opt. Express*, vol. 25, no. 1, pp. 191–201, Jan. 2017.

[47] C.-C. Chang, L. Huang, J. Nogan, and H.-T. Chen, "Invited article: Narrowband terahertz bandpass filters employing stacked bilayer metasurface antireflection structures," *APL Photon.*, vol. 3, no. 5, May 2018, Art. no. 051602.

[48] S. Biabanifard, M. Biabanifard, S. Asgari, S. Asadi, and M. C. E. Yagoub, "Tunable ultra-wideband terahertz absorber based on graphene disks and ribbons," *Opt. Commun.*, vol. 427, pp. 418–425, Nov. 2018.
[49] M. Biabanifard, A. Arsanjani, M. S. Abrishamian, and D. Abbott, "Tunable terahertz graphene-based absorber design method based on a circuit model approach," *IEEE Access*, vol. 8, pp. 70343–70354, 2020.
[50] A. Najafi, M. Soltani, I. Chaharmahali, and S. Biabanifard, "Reliable design of THz absorbers based on graphene patterns: Exploiting genetic algorithm," *Optik*, vol. 203, Feb. 2020, Art. no. 163924.
[51] X. F. Fan, W. T. Zheng, V. Chihaia, Z. X. Shen, and J.-L. Kuo, "Interaction between graphene and the surface of SiO2," *J. Phys., Condens. Matter*, vol. 24, no. 30, Aug. 2012, Art. no. 305004.
[52] X. H. Deng, J.-T. Liu, J. Yuan, T.-B. Wang, and N.-H. Liu, "Tunable THz absorption in graphene-based heterostructures," *Opt. Express*, vol. 22, no. 24, pp. 30177–30183, 2014.
[53] G. Kedawat, S. Srivastava, V. K. Jain, P. Kumar, V. Kataria, Y. Agrawal, B. K. Gupta, and Y. K. Vijay, "Fabrication of artificially stacked ultrathin ZnS/MgF_2 Multilayer dielectric optical filters," *ACS Appl. Mater. Interface*, vol. 5, no. 11, pp. 4872–4877, Jun. 2013.
[54] I. Khromova, A. Andryieuski, and A. Lavrinenko, "Ultrasensitive terahertz/infrared waveguide modulators based on multilayer graphene metamaterials," *Laser Photon. Rev.*, vol. 8, no. 6, pp. 916–923, Nov. 2014.
[55] M. Liu, X. Yin, E. Ulin-Avila, B. Geng, T. Zentgraf, L. Ju, F. Wang, and X. Zhang, "A graphene-based broadband optical modulator," *Nature*, vol. 474, no. 7349, pp. 64–67, Jun. 2011.
[56] Q. Gong, and X. Hu, Eds., *Photonic Crystals: Principles and Applications*. Stanford, CA, USA: PAN Stanford, 2014.
[57] K. Petritsch, *Photonic Crystals—Introduction, Theory and Applications*. Burlington, ON, Canada: Arcler Press LLC, 2017.
[58] A. H. C. Neto, F. Guinea, N. M. R. Peres, K. S. Novoselov, and A. K. Geim, "The electronic properties of graphene," *Rev. Mod. Phys.*, vol. 81, no. 1, pp. 109–162, 2009.
[59] G. W. Hanson, "Dyadic green's functions and guided surface waves for a surface conductivity model of graphene," *J. Appl. Phys.*, vol. 103, no. 6, Mar. 2008, Art. no. 064302.
[60] Z. Liu, K. Suenaga, P. J. F. Harris, and S. Iijima, "Open and closed edges of graphene layers," *Phys. Rev. Lett.*, vol. 102, no. 1, Jan. 2009, Art. no. 015501.
[61] K. Yan, H. Peng, Y. Zhou, H. Li, and Z. Liu, "Formation of bilayer bernal graphene: Layer-by-layer epitaxy via chemical vapor deposition," *Nano Lett.*, vol. 11, no. 3, pp. 1106–1110, Mar. 2011.
[62] I.-T. Lin, J.-M. Liu, K.-Y. Shi, P.-S. Tseng, K.-H. Wu, C.-W. Luo, and L.-J. Li, "Terahertz optical properties of multilayer graphene: Experimental observation of strong dependence on stacking arrangements and misorientation angles," *Phys. Rev. B, Condens. Matter*, vol. 86, no. 23, Dec. 2012, Art. no. 235446.
[63] M. A. K. Othman, C. Guclu, and F. Capolino, "Graphene-based tunable hyperbolic metamaterials and enhanced near-field absorption," *Opt. Express*, vol. 21, no. 6, pp. 7614–7632, 2013.
[64] S. Shi, C. Chen, and D. W. Prather, "Plane-wave expansion method for calculating band structure of photonic crystal slabs with perfectly matched layers," *J. Opt. Soc. Amer. A, Opt. Image Sci.*, vol. 21, pp. 1769–1775, Sep. 2004.
[65] Y.-J. Gao, H.-W. Yang, and G.-B. Wang, "A research on the electromagnetic properties of plasma photonic crystal based on the symplectic finite-difference time-domain method," *Optik*, vol. 127, no. 4, pp. 1838–1841, Feb. 2016.
[66] A. Madani and S. Roshan Entezar, "Surface polaritons of one-dimensional photonic crystals containing graphene monolayers," *Superlattices Microstruct.*, vol. 75, pp. 692–700, Nov. 2014.
[67] Y. Li, L. Qi, J. Yu, Z. Chen, Y. Yao, and X. Liu, "One-dimensional multi-band terahertz graphene photonic crystal filters," *Opt. Mater. Express*, vol. 7, no. 4, pp. 1228–1239, 2017.
[68] N. Ouchani, D. Bria, B. Djafari-Rouhani, and A. Nougaoui, "Defect modes in one-dimensional anisotropic photonic crystal," *J. Appl. Phys.*, vol. 106, no. 11, Dec. 2009, Art. no. 113107.
[69] N. Ouchani, A. El Moussaouy, H. Aynaou, Y. El Hassouani, E. H. El Boudouti, and B. Djafari-Rouhani, "Optical transmission properties of an anisotropic defect cavity in one-dimensional photonic crystal," *Phys. Lett. A*, vol. 382, no. 4, pp. 231–240, Jan. 2018.
[70] A. A. Sayem, M. M. Rahman, M. R. C. Mahdy, I. Jahangir, and M. S. Rahman, "Negative refraction with superior transmission in graphene-hexagonal boron nitride (hBN) multilayer hyper crystal," *Sci. Rep.*, vol. 6, no. 1, Jul. 2016.
[71] D. Rodrigo, A. Tittl, O. Limaj, F. J. G. de Abajo, V. Pruneri, and H. Altug, "Double-layer graphene for enhanced tunable infrared plasmonics," *Light, Sci. Appl.*, vol. 6, no. 6, p. 16277, 2017.
[72] S.-X. Xia, X. Zhai, L.-L. Wang, B. Sun, J.-Q. Liu, and S.-C. Wen, "Dynamically tunable plasmonically induced transparency in sinusoidally curved and planar graphene layers," *Opt. Express*, vol. 24, no. 16, pp. 17886–17899, 2016.
[73] H.-C. Hung, C.-J. Wu, and S.-J. Chang, "Terahertz temperature-dependent defect mode in a semiconductor-dielectric photonic crystal," *J. Appl. Phys.*, vol. 110, no. 9, Nov. 2011, Art. no. 093110.

M. POURMAND received the B.Sc. degree in electrical engineering from the Khajeh Nasirodin Toosi University of Technology, Iran, in 2004, and the M.Sc. degree in electrical engineering from the Tafresh University, Iran, in 2013. From 2004 to 2020, he worked as an electronic engineer at industry sector. He is currently a Doctoral Student with the Institute of Microengineering and Nanoelectronics, Universiti Kebangsaan Malaysia (The National University of Malaysia, Malaysia). His research interests lie in metamaterials, photonic crystals and plasmonics from fundamental as well as practical perspectives.

P. K. CHOUDHURY (Senior Member, IEEE) received the Ph.D. degree in physics, in 1992. He held academic positions in India, Canada, Japan, and Malaysia. From 2003 to 2009, he was a Professor with the Faculty of Engineering, Multimedia University, Cyberjaya, Malaysia. Thereafter, he joined professorship at the Institute of Microengineering and Nanoelectronics, Universiti Kebangsaan Malaysia, Malaysia. Also, he served the Telekom Research and Development (TMR&D, Malaysia) as a consultant for a couple of projects on optical devices. His research interests lie in the theory of optical waveguides, which include complex mediums, fiber optic devices, optical sensors and metamaterial properties. He has published over 250 research papers, contributed chapters to 14 books, and edited and co-edited 06 research level books. He is the reviewer for over three dozen research journals. Also, he is the Section Editor of Optik – International Journal for Light and Electron Optics, Elsevier, The Netherlands, and the Editor-in-Chief of the Journal of Electromagnetic Waves and Applications (Taylor & Francis, U.K.). He is Senior Member of OSA and SPIE.